

Molecular wave-packet dynamics on laser-controlled transition states

Andreas Fischer,^{1,*} Martin Gärtner,¹ Philipp Cörlin,¹ Alexander Sperl,¹ Michael Schönwald,¹ Tomoya Mizuno,¹ Giuseppe Sansone,² Arne Senftleben,³ Joachim Ullrich,⁴ Bernold Feuerstein,¹ Thomas Pfeifer,¹ and Robert Moshhammer^{1,†}

¹*Max-Planck-Institut für Kernphysik, Saupfercheckweg 1, 69117 Heidelberg, Germany*

²*Dipartimento di Fisica, Politecnico Milano, Piazza Leonardo da Vinci 32, 20133 Milano, Italy*

³*Institut für Physik, Universität Kassel, Heinrich-Plett-Straße 40, 34132 Kassel, Germany*

⁴*Physikalisch-Technische Bundesanstalt, Bundesallee 100, 38116 Braunschweig, Germany*

(Received 26 June 2015; published 13 January 2016)

We present a kinematically complete and time-resolved study of the dissociation dynamics of H_2^+ using ultrashort extreme-ultraviolet and near-infrared laser pulses. The reaction kinematics can be controlled by varying the time delay between the two pulses. We demonstrate that a time-dependent laser-dressed potential-energy curve enables the control of the nuclear motion. The dynamics is well reproduced by intuitive semiclassical trajectories on a time-dependent potential curve. From this most fundamental scenario we gain insight in the underlying mechanisms which may be applied as design principles for molecular quantum control, particularly for ultrafast molecular reactions involving the motion of protons.

DOI: [10.1103/PhysRevA.93.012507](https://doi.org/10.1103/PhysRevA.93.012507)

I. INTRODUCTION

Understanding and controlling the electronic as well as rovibrational motion and thus the entire chemical dynamics in molecular reactions is the ultimate goal of ultrafast laser and imaging science [1,2]. In photochemistry, laser-induced dissociation has become a valuable tool for the modification of reaction pathways and kinetics science [1–9]. In many control schemes, dissociation is achieved by laser-induced coupling of two electronic states, leading to the formation of light-induced potential-energy surfaces (LIPs) [9–12].

Analogous to catalysis in chemistry, “laser catalysis” serves to lower the potential barrier between reactants and products [2]. It has even been demonstrated that, by using evolutionary algorithms, light pulses can be shaped to induce a desired reaction, e.g., Refs. [13–17]. The complexity of molecular systems, however, is the main challenge towards comprehensive molecular laser control and the required understanding of the corresponding dynamical mechanisms. This complexity stems from the vast number of degrees of freedom of polyatomic molecules—including electronic, vibrational, and possibly rotational states—which have to be controlled. In addition, laser pulses for creating LIPs operate in the strong-field regime, where nonlinear dependencies on the laser intensity and pulse duration are encountered.

In view of this complexity, it is essential to understand and to analyze the underlying mechanisms first for most basic systems. Here, we use the molecular hydrogen ion H_2^+ as it represents the most fundamental testbed for quantum control of ultrafast molecular motion.

In this paper, we combine attosecond spectroscopy and strong laser control to explore and understand the dynamics of a wave packet on a time-dependent IR-laser-dressed LIP via an XUV pump–IR control experiment [see Figs. 1(a) and 2]. We observe that the kinetic-energy distribution of the reaction products sensitively depends on the time delay between the

pump and control pulse, as shown in Fig. 1(b). This means that the kinetic energy of the fragments can be controlled by changing the time delay. We analyze the measured spectra in detail by applying a Fourier-transform technique and by comparing to extensive wave-packet dynamics simulations. This shows that the dissociation process can be described in terms of wave-packet motion on a single LIP. It turns out that the fragment kinetic energy depends on whether the vibrational wave packet experiences an increasing or decreasing (with time) potential barrier during the dissociation, as illustrated in Fig. 1(b). This semiclassical picture provides an intuitive understanding of the underlying mechanism which we dub the “elevator” effect.

II. EXPERIMENTAL SETUP

In the experiment we use a commercially available ring amplifier which yields laser pulses with a temporal duration of 25 ± 5 fs and with a center wavelength of 780 nm at a repetition rate of 8 kHz. These pulses are spectrally broadened within a neon-filled hollow-core fiber and subsequently temporally recompressed to 9 fs using chirped mirrors.

The pulses are divided in a pump pulse and a control pulse using a beam splitter within a vacuum chamber (see Fig. 2). One beam path (the left interferometer path in Fig. 2 labeled “XUV path”) is used to create APTs via the high-order harmonic generation (HHG) [18–23]. For this, the pulse is focused into an gas cell filled with argon (see “HHG target” in Fig. 2). A subsequent aluminum filter separates the APTs, which have photon energies ranging from 17 to approximately 40 eV, from the generating IR light. Finally, the APTs are focused into the reaction microscope.

The length of the second interferometer path is adjustable using a retroreflector mounted on a piezo-controlled delay stage. With this, very large delays of up to 10 ps can be introduced between the two pathways. Furthermore, using a motorized iris aperture, the intensity of the pulses propagating along this interferometer arm can be controlled.

Using a drilled parabolic mirror, both beam paths are spatially overlapped. This mirror further focuses the IR pulse

*andreas.fischer@mpi-hd.mpg.de

†robert.moshhammer@mpi-hd.mpg.de

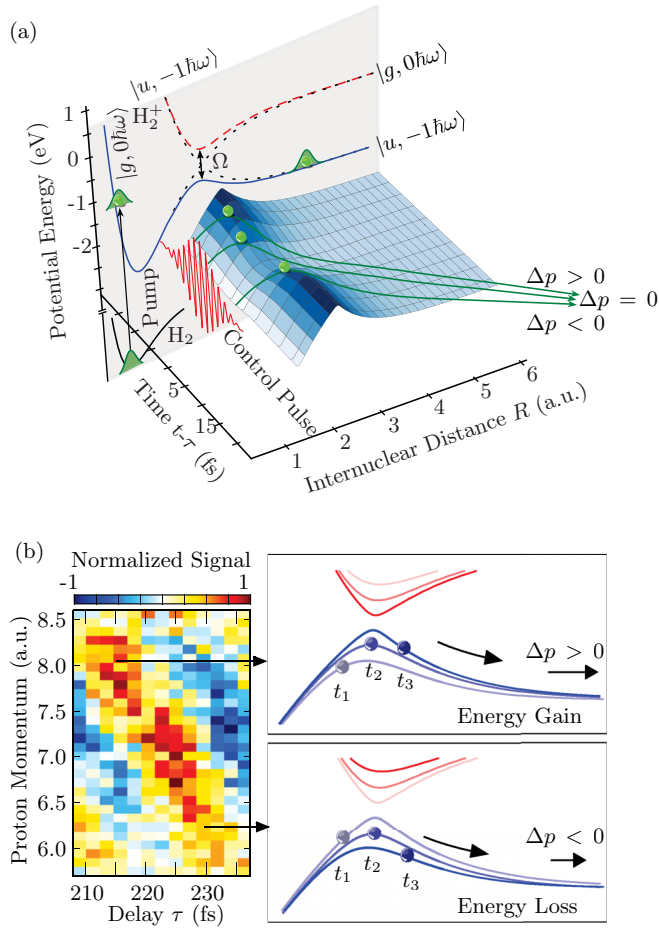


FIG. 1. (a) Background: The pump pulse ionizes neutral H_2 , preparing a vibrational wave packet in the H_2^+ ground state $|g\rangle$. The time-delayed control pulse couples $|g\rangle$ to the dissociative $|u\rangle$ state. Blue solid and red dashed curves show the relevant LIPs (Floquet picture). The opening Ω of the resulting avoided crossing (i.e., the height of the dissociation barrier) depends on the coupling laser intensity. Foreground: The blue surface shows the time evolution of the lower LIP. The envelope of the control pulse leads to a time-dependent lowering of the dissociation barrier. Depending on the time delay τ , the dissociating fragments either gain or lose energy while traversing the barrier (three example trajectories are shown). (b) Left: Measured proton count distribution as function of momentum and delay. For this figure, the signal's average along the delay axis was subtracted for each proton momentum. This allows a comparison to the later applied Fourier analysis. Right: As a function of the time delay, the final proton momentum changes significantly. This can be understood in terms of an upward and downward moving LIP while the wave packet is traversing the barrier. These illustrations show the behavior of the LIP along the classical trajectories plotted in (a) labeled $\Delta p > 0$ and $\Delta p < 0$.

(the attosecond pulses are already focused) in the center of a reaction microscope [24] intersecting a supersonic jet of hydrogen gas. The hydrogen molecules are ionized by the APT (pump pulse) launching nuclear dynamics. By applying the fundamental IR pulse (control pulse) at a variable time delay τ after the pump pulse, the molecular ion is dissociated and the fragmentation dynamics is influenced. Using a reaction

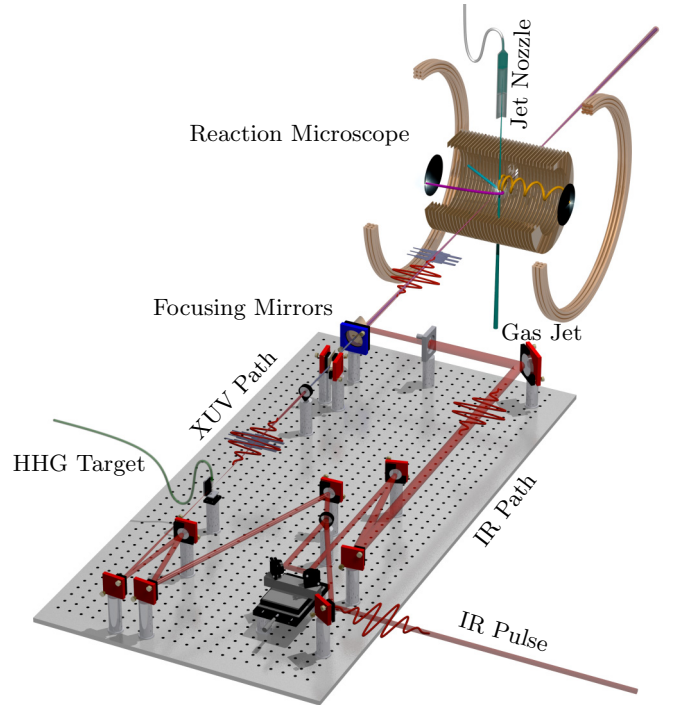
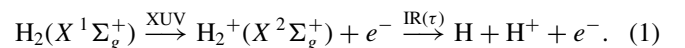


FIG. 2. Illustration of the experimental setup. A near-infrared (IR) laser pulse is split into two using a broadband beam splitter. One copy of the laser pulse is used to create the attosecond pulse trains (APTs) in the high-order harmonic generation process in an argon HHG target. Subsequently, the APTs are focused, in the center of the reaction microscope, into a supersonic jet of molecular hydrogen. The other copy of the IR pulse is time delayed, and, collinearly to the APTs, focused into the reaction microscope.

microscope we obtain the full kinematic information of the process under investigation [24].

III. EXPERIMENTAL RESULTS

We consider the following reaction describing dissociative photoionization in a two-pulse experiment:



As a result of the ionization, many vibrational levels of the $H_2^+(X^2\Sigma_g^+)$ state (in the following called $|g\rangle$) are excited, according to the Franck-Condon overlap with the ground-state nuclear wave function in the $|g\rangle$ potential. The IR control pulse [see Fig. 1(a)], which is polarized parallel to the XUV pulse, couples the $|g\rangle$ and the $H_2^+(A^2\Sigma_u^+)$ state ($|u\rangle$) and causes the molecule to dissociate. This scheme thus enables us to monitor and influence the time evolution of the vibrational wave packet by varying the time delay τ between the pump and the control pulse [illustrated in Fig. 1(a)].

Figure 1(b) shows the measured H^+ yield as a function of the proton momentum p integrated over all molecular orientations and the time delay τ for only one oscillation period of the vibrational wave packet. To allow for a comparison to the results of the later presented analysis, the average value along the time-delay axis is subtracted individually for each measured

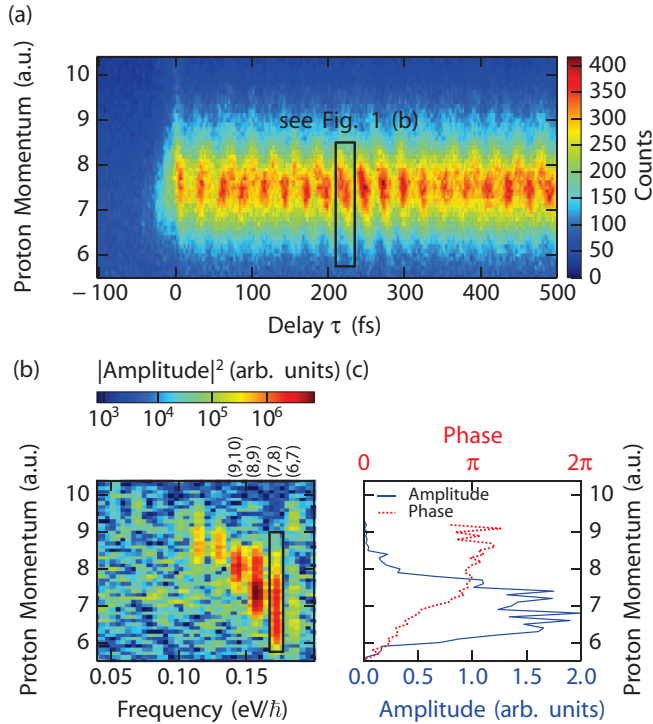


FIG. 3. (a) Measured proton count distribution $C(p, \tau)$ as a function of momentum and delay. A pronounced oscillation is visible. The black frame marks the data shown in Fig. 1(b). (b) The Fourier transform $F(p, \omega)$ of $C(p, \tau)$ along the time-delay axis is shown. Clearly visible are the lines belonging to the beating of two adjacent vibrational states. (c) The amplitude (solid line) and phase (dotted line) of the vibrational states $v = (7, 8)$ as a function of the proton momentum. With increasing proton momentum, a phase change of approximately π is observed.

proton momentum. This accounts for the fact that later we employ a Fourier transform with which we can select individual beat frequencies at the cost of losing the zero-frequency part of the signal, which corresponds to the average value along the time axis. A clear dependency of the proton momenta on the time delay is visible [see Fig. 1(b) arrows]. This dependence is the key aspect and throughout this paper will be explained in terms of time-dependent LIPs [illustrated on the right-hand side of Fig. 1(b)] which are traversed on the time scale on the order of the IR control pulse duration. The fact that the duration of the IR control pulse is on the same time scale as the dissociation through the coupling region is an essential aspect of this work. To give a better overview of the results, Fig. 3(a) shows the measured H^+ counts $C(p, \tau)$ for a larger time-delay range (we show only 600 fs of the totally measured 1007 fs delay range for better visibility of the features). $\tau < 0$ corresponds to the case where the IR pulse precedes the XUV pulse. A pronounced oscillation as a function of the time delay τ with an approximate period of 26 fs is visible. This oscillation reflects the time evolution of a wave packet that can be described by a superposition of vibrational states. Due to the anharmonicity of the $|g\rangle$ potential, the energy spacings of different pairs of states are not equal, which causes the observed oscillation to dephase and rephase, visible as periodic variations in the contrast of the oscillation (nuclear

wave-packet revival). Figure 3(b) shows the Fourier transform $F(p, \omega)$ of the count distribution $C(p, \tau)$ with respect to the time delay. By comparing the energy spacings between the calculated vibrational states in the $|g\rangle$ potential, we assign a pair of contributing vibrational states to each line visible in Fig. 3(b).

The aspect of revivals of the oscillation signal in the time and frequency domain has been subject to numerous studies (see, e.g., Refs. [25–33]). Here, we focus on phase-dependent features (occurring on the time scale of a single cycle of the vibrational wave-packet motion), describing the dynamics of the dissociation process (see Sec. V).

In order to achieve an understanding of this dynamics, we have performed numerical wave-packet dynamics simulations. For this, the following time-dependent Schrödinger equation (TDSE) (in atomic units) was solved,

$$i \frac{d}{dt} \begin{pmatrix} \Psi_1(t) \\ \Psi_2(t) \end{pmatrix} = \begin{pmatrix} \frac{\hat{p}^2}{2\mu} + V_g & -D \times E(t) \\ -D \times E(t) & \frac{\hat{p}^2}{2\mu} + V_u \end{pmatrix} \begin{pmatrix} \Psi_1(t) \\ \Psi_2(t) \end{pmatrix}, \quad (2)$$

using the split-operator technique [34], where V_g and V_u are the potential energies of the $|g\rangle$ and the $|u\rangle$ state, respectively, D is the electronic dipole moment coupling the two states, and $E(t) = E_{\parallel} G(t - \tau) \cos(\omega t)$ is the component of the control laser field parallel to the internuclear axis with the Gaussian envelope $G(t)$. In this, $\Psi_1(R, t)$ and $\Psi_2(R, t)$ were treated to be one-dimensional wave functions. As this neglects rotational aspects and alignment induced by the control pulse, this cannot be a complete description. However, for the framework of this paper, it is a sufficient model. The initial state is assumed to be the Franck-Condon wave packet, i.e., the H_2 ground state promoted vertically to the $|g\rangle$ manifold. At long times $t_f \gg \tau$, the dissociating part (mainly propagating on the $|u\rangle$ manifold) of the wave function is well separated from the remaining bound part and its momentum distribution can be extracted. Using $E_{\parallel} = E_0 \cos(\theta)$ and adjusting only E_0 (i.e., the peak intensity of the control pulse $I_0 = \frac{1}{2} \epsilon_0 c E_0^2$) and the pulse length, we obtain excellent agreement with the experimental results.

IV. INTENSITY DEPENDENCE

In the following, we demonstrate that we are able to study the influence of the IR-pulse intensity on the dissociation dynamics of the molecular hydrogen ion by selecting events in which the molecular axis is oriented at a specific angle θ to the polarization of the control laser field. Due to the dipole selection rules between the two states, only parallel transitions, in which the molecular axis is oriented parallel to the effective electric field of the coupling laser, are allowed. Hence, the states $|g\rangle$ and $|u\rangle$ are coupled solely by the electric field component parallel to the molecular axis (which leads to a mixing of Ψ_1 and Ψ_2). Thus, by selecting events in which the proton was detected under an angle θ with respect to the laser polarization, the effective laser intensity is reduced to $I_{\text{eff}} = I_0 \cos^2(\theta)$. Figure 4 shows the resulting Fourier spectra for three angles, i.e., increasing effective intensities from top to bottom, where the alignment was chosen to be in the intervals $0.2 < \cos(\theta) < 0.4$, $0.65 < \cos(\theta) < 0.75$, and $\cos(\theta) > 0.9$, in Figs. 4(a) and 4(b), Figs. 4(c) and 4(d), and

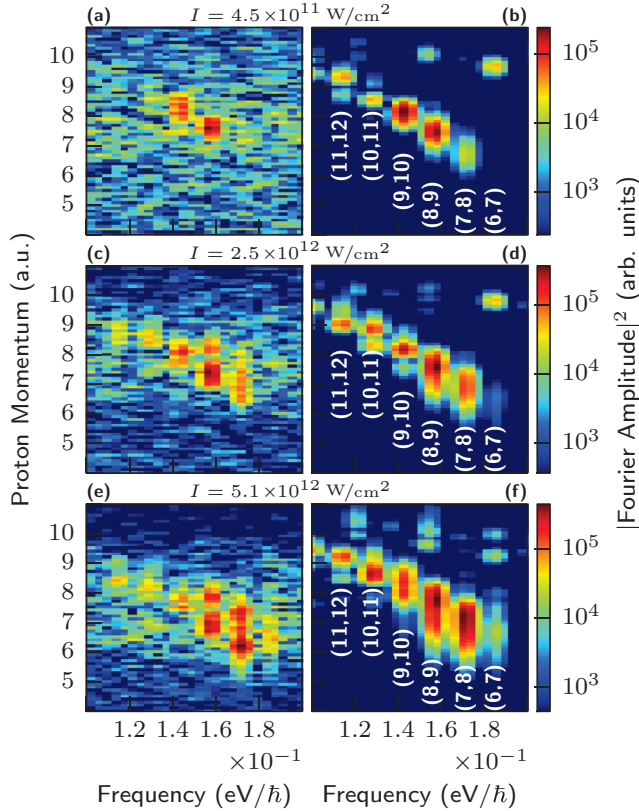


FIG. 4. Fourier transforms of the time-dependent count distribution for different effective laser intensities. The laser intensity increases from top to bottom. Left column: The obtained experimental data. Right column: The theoretical calculation using the TDSE is shown. With increasing field strength, lower vibrational states get involved in the dissociation process. The pulse duration is $\sigma_{\text{FWHM}} = 8.6$ fs with a center wavelength of $\lambda = 760$ nm.

Figs. 4(e) and 4(f), respectively. Very good agreement between experimental data and the results of our quantum wave-packet dynamics simulation is found, which validates the chosen approach of selecting different effective intensities.

The adjusted intensity $I_0 = 5.1 \times 10^{12}$ W/cm² and temporal pulse length $\sigma_{\text{FWHM}} = 8.6$ fs of the laser pulse used in the simulation are consistent with our experimental parameters. The center wavelength $\lambda = 760$ nm was determined from measured electron momentum distributions (not shown in this paper).

V. WATCHING WAVE PACKETS TRAVERSE LASER-INDUCED TRANSITION STATES USING FOURIER ANALYSIS

Experimental results and their evaluation investigating the quantum beat signals and revivals have already been reported in previous works, e.g., Refs. [26,27,29,30,32]. In this section we present an assessment of this transition state dynamics, which constitutes the main result of our work.

The key to access the dynamical information is the phase of the Fourier coefficients [dotted line in Fig. 3(c)]. To illustrate the meaning of these phases we select a single line of the Fourier spectrum [e.g., the black box in Fig. 3(b)], corresponding to two vibrational states ν_1 and ν_2 , and perform an inverse

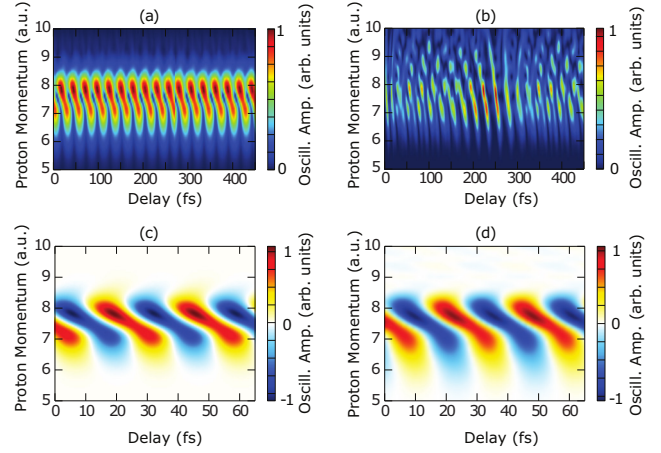


FIG. 5. Comparison between the dynamics of two vibrational states and the Fourier filtered signal. This proves that the Fourier ansatz is valid and can be used in order to observe the time dynamics of only two coherently excited states. Left column: Simulated count distribution resulting from the preparation of a wave packet consisting of two vibrational states ($\nu = 8$ and 9). (a) Bare spectrum and (c) spectrum after subtraction of the dc component. Right column: (b) Count distribution for the full Franck-Condon wave packet. (d) Result of the Fourier analysis. After the inverse transformation of the corresponding line in the Fourier spectrum to the time domain, the “two-state” signal is obtained.

Fourier transform back to the time domain (wavelet analysis) [see Fig. 6(a)]. This way, we isolate the part of the time-delay spectrum that is oscillating with frequency $(E_{\nu_2} - E_{\nu_1})/\hbar$. Physically, this signal corresponds to the result that would be obtained if a superposition of only two isolated vibrational states was prepared in the first place. In order to demonstrate that the signal obtained by our Fourier filtering technique is indeed equivalent to the signal one would obtain by preparing and probing a single pair of vibrational states, we compare the outcomes of wave-packet dynamics simulations for two different cases: First, we prepare a superposition of two vibrational states, which we propagate by solving the time-dependent Schrödinger equation (details of the methodology can be found in Ref. [35]). The resulting count distribution is shown in Fig. 5(a). As expected, the obtained distribution is perfectly periodic linewise for each proton momentum. Again, for comparability to the wavelet analysis, we subtracted the average along the time axis from the signal (which is equal to omitting the zero-frequency component in the wavelet analysis as it has to be done in the data evaluation) and obtain Fig. 5(c). Second, we simulate the full wave-packet dynamics, taking into account all populated vibrational states according to their Franck-Condon overlap to the neutral ground-state wave function and then apply the wavelet analysis technique [see Fig. 5(b)]. The resulting filtered signal [Fig. 5(d)] is in very good agreement with the beating signal of two states after subtraction of the dc component [Fig. 5(c)]. The fact that the two approaches yield very similar results [compare Figs. 5(c) and 5(d)] validates our approach on isolating pairs of vibrational states.

Figure 6 depicts the results of this wavelet analysis for two different laser intensities ($I_1 = 5.1 \times 10^{12}$ W/cm² and $I_2 = 4.5 \times 10^{11}$ W/cm²). For the case of I_1 [(a)–(d)] the

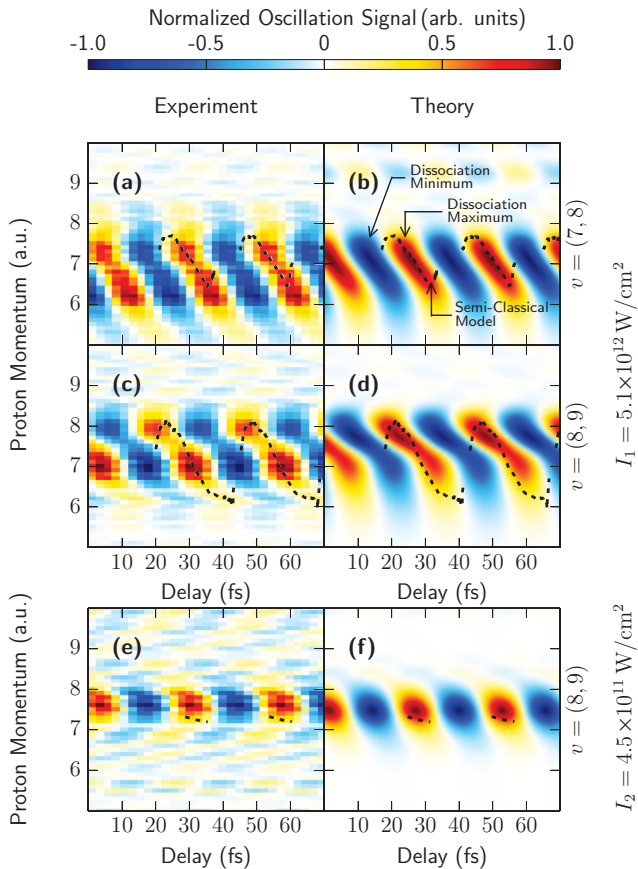


FIG. 6. Analysis of lines corresponding to the pairs of vibrational states $v = (7,8)$ and $v = (8,9)$ for two different effective laser intensities [(a)–(d) $I_1 = 5.1 \times 10^{12}$ W/cm² and (e), (f) $I_2 = 4.5 \times 10^{11}$ W/cm²]. Left column: The experimental data. Right column: Wave-packet dynamics simulation. For the intensity I_2 , the dissociation probability of the states $v = (8,9)$ is vanishingly small, hence we omitted the plot. The signal average along the time axis is subtracted and the spectra are normalized to values between -1 and 1 , where -1 corresponds to the smallest dissociation amplitude and 1 to the largest. The dotted lines show the proton momentum as a function of time delay τ predicted by the semiclassical simulation (see text).

delay-dependent proton momentum is shown for two selected pairs of vibrational states, namely, $v = (7,8)$ and $v = (8,9)$. The deeper bound vibrational state pair $v = (7,8)$ is no longer dissociated for the case of I_2 , hence we only show the signal corresponding to the state pair $v = (8,9)$ [Fig. 6(e) and 6(f)]. For increasing intensity, we observe a broadening of the proton momentum distribution. This implies that for high-field strengths we enter a regime in which the time scale of laser-induced potential barrier modification and the traversal time of the wave packet across the barrier are comparable, and thus the kinetic energy of the fragments can be altered during the transition. In this regime, the final fragment momentum decreases as a function of the time delay τ with a period corresponding to the quantum-mechanical wave-packet oscillation. The mechanism responsible for the (oscillatory) time and intensity dependence of the final proton momentum can be understood in terms of a semiclassical model which we discuss in the following.

For the understanding of the model, we first note that it is useful to employ a Floquet-state picture. We have verified numerically that for our laser parameters the molecules almost exclusively dissociate on the $|u, -1\hbar\omega\rangle$ manifold (see Ref. [35] for details of the methodology). We therefore assume that the wave-packet dynamics in the control field follows the $|g, 0\hbar\omega\rangle$ manifold, except at the one-photon avoided crossing where it follows the potential-energy curve $V_1(R, t)$ connected to the $|u, -1\hbar\omega\rangle$ asymptote. The relevant curves are illustrated in Fig. 1(a). In our semiclassical model we now propagate a classical particle on the energetically lower LIP $V_1(R, t)$ by solving Newton’s equation for the time-dependent potential. The particle is initially at rest at the left turning point r_0 , energetically corresponding to the mean value of the binding energies of the corresponding vibrational states $V_1(R_0, 0) = (E_{v_2} + E_{v_1})/2$. Depending on the time at which the control pulse arrives, the particle can pass the potential barrier and exit, or it remains bound. We also find that its final momentum $p(t \rightarrow \infty)$ depends on the time delay of the control pulse and thus on the phase of the particle oscillation at the time the strong-field pulse arrives. This is illustrated by the arrows in Fig. 1(a), and the quantitative results of the simulated time-delay-dependent final momenta are represented by the dotted lines in Fig. 6. For the vibrational states $v = (7,8)$ and $v = (8,9)$, the final proton momenta as a function of delay in experiment, theory, and the classical expectation agree very well. In particular, the periodic momentum decrease with increasing time delay is reproduced. Note that, due to the large binding energy of the vibrational states $v = (6,7)$, the semiclassical model fails in this case, as the protons are classically not freed at the corresponding laser intensity. In contrast, quantum mechanically, the molecule may dissociate due to the finite width of the quantum-mechanical wave packet’s momentum spread.

Using the time-dependent LIP picture, we are thus able to explain the mechanism that causes the proton’s time-delay-dependent momentum. For this, we first note that the LIP in the transition state (coupling region) can be regarded as an “elevator.” During the interaction with the coupling laser it moves down for increasing laser intensity and up again for decreasing laser intensity. This up and down motion of the “elevator” happens on the same time scale on which the particles traverse the coupling region. This results in a change of total energy of the dissociating molecule. To clarify this mechanism we consider two cases, which lead to a loss and to a gain of final kinetic energy, respectively. First, the particles enter the downward-moving potential barrier and exit it close to its lowest point, and are therefore losing energy. This case is illustrated in Fig. 1(a) by the arrow labeled $\Delta p < 0$ and in the lower right-hand panel of Fig. 1(b). In the second case, the particles traverse the coupling region while the potential moves upward and the nuclei gain energy [illustrated in Fig. 1(a) by the arrow labeled $\Delta p > 0$ and in the upper right-hand panel of Fig. 1(b)]. This means that the coupling laser field acts as a control knob to accelerate or decelerate the nuclei during the molecular dissociation reaction depending on the relative phase between the wave-packet oscillation and the arrival of the coupling pulse.

This mechanism is further illustrated in the Supplemental Material [36] (movies S1–S3 and movie S4). Movie S1

illustrates the elevator mechanism as acting in the semiclassical model for the case of a gain of total energy. The final velocity of the observed proton is the highest for this case. Movie S2 presents the case of a loss of total energy followed by a regain. The net change of the total energy vanishes. In movie S3, finally the case of an energy loss resulting in the lowest final velocity of the observed proton is shown.

VI. CONCLUSION

In conclusion, we have demonstrated strong-field-induced kinetic-energy control of molecular reaction products in an XUV-pump IR-probe experiment. We find an “elevator” mechanism to be responsible for the control of the reaction pathway through a laser-induced transition state. A semiclassical model describes and predicts the mean behavior of the momentum distribution surprisingly well, even though the corresponding wave packets consist of only two vibrational states. The fact that the wave-packet dynamics for light molecules such as H_2^+ , where quantum effects are expected to be most significant, can be understood in terms of semiclassical modeling might offer a broad applicability of the model to more complex processes in quantum control. Especially for larger molecules, where a complete quantum-mechanical modeling is difficult if not impossible, the validity of semiclassical mechanisms might be the key to reduce the complexity of the system’s description. The control over internuclear momenta (and thus internuclear kinetic energies) by the discovered “elevator” mechanism promises an efficient approach to specifically address different intermediate and final states, even in nondissociating scenarios.

ACKNOWLEDGMENTS

We thank Uwe Thumm, Sebastian Meuren, and Andreas Kaldun for fruitful discussions. T.M. is grateful for the financial support of a JSPS Fellowship for Research Abroad.

G.S. acknowledges financial support by the Alexander von Humboldt Foundation (Project “Tirint”).

APPENDIX: DESCRIPTION OF SUPPLEMENTAL MATERIAL

The above described mechanism is further illustrated in the Supplemental Material [36] (movies S1–S3 and movie S4). Movie S1 illustrates the elevator mechanism as acting in the semiclassical model for the case of a gain of total energy. The final velocity of the observed proton is the highest for this case. Movie S2 presents the case of a loss of total energy, followed by a regain. The net change of the total energy vanishes. In movie S3, finally, the “downward elevator” case of an energy loss resulting in the lowest final velocity of the observed proton is shown.

In order to give an improved comparability of the semiclassical model to the quantum-mechanical simulations, movie 4 features both representations in the coordinate and momentum space. It illustrates the elevator mechanism as acting in the semiclassical model for the case of a superposition of the vibrational states $v = 7$ and $v = 8$. We show the time evolution of quantum-mechanical wave packets of the bound and dissociating component (blue and orange), the expectation values of the position operator, and the position of a classical particle moving on the Floquet potential adiabatically connecting the two. The size (area) of the blue and orange dots reflects the norm of the respective components. Three cases, corresponding to three different delays, are shown. Top row: The transition over the barrier takes place while it rises (the IR-pulse amplitude decreases). The final velocity p_{cl} of the proton is highest. The total energy E_{tot} increases during the dissociation process. Middle row: While traversing the barrier the particle experiences both a decreasing and increasing potential. The net change in total energy is small. Bottom row: The particle moves across a decreasing barrier, thereby losing energy. The quantum-mechanical expectation value of the velocity of the dissociating component $p_{qm,2}$ follows this trend.

-
- [1] A. H. Zewail, *J. Phys. Chem. A* **104**, 5660 (2000).
 - [2] M. Shapiro and P. Brumer, *J. Chem. Soc., Faraday Trans.* **93**, 1263 (1997).
 - [3] M. E. Corrales, J. Gonzalez-Vázquez, G. Balerdi, I. R. Solá, R. de Nalda, and L. Bañares, *Nat. Chem.* **6**, 785 (2014).
 - [4] B. J. Sussman, D. Townsend, M. Y. Ivanov, and A. Stolow, *Science* **314**, 278 (2006).
 - [5] C. Daniel, J. Full, L. González, C. Lupulescu, J. Manz, A. Merli, Å. Vajda, and L. Wöste, *Science* **299**, 536 (2003).
 - [6] M. E. Corrales, V. Lorient, G. Balerdi, J. Gonzalez-Vazquez, R. de Nalda, L. Bañares, and A. H. Zewail, *Phys. Chem. Chem. Phys.* **16**, 8812 (2014).
 - [7] A. Assion, T. Baumert, M. Bergt, T. Brixner, B. Kiefer, V. Seyfried, M. Strehle, and G. Gerber, *Science* **282**, 919 (1998).
 - [8] J. González-Vázquez, L. González, S. R. Nichols, T. C. Weinacht, and T. Rozgonyi, *Phys. Chem. Chem. Phys.* **12**, 14203 (2010).
 - [9] E. E. Aubanel and A. D. Bandrauk, *J. Phys. Chem.* **97**, 12620 (1993).
 - [10] H. Rabitz, R. de Vivie-Riedle, M. Motzkus, and K. Kompa, *Science* **288**, 824 (2000).
 - [11] D. J. Tannor, *Nature (London)* **369**, 445 (1994).
 - [12] C. Truemp, H. Rottke, M. Wittmann, G. Korn, W. Sandner, M. Lein, and V. Engel, *Phys. Rev. A* **62**, 063402 (2000).
 - [13] A. M. Weiner, *Rev. Sci. Instrum.* **71**, 1929 (2000).
 - [14] A. M. Weiner, D. E. Leaird, G. P. Wiederrecht, and K. A. Nelson, *Science* **247**, 1317 (1990).
 - [15] W. Jakubetz, J. Manz, and H.-J. Schreier, *Chem. Phys. Lett.* **165**, 100 (1990).
 - [16] R. S. Judson and H. Rabitz, *Phys. Rev. Lett.* **68**, 1500 (1992).
 - [17] W. S. Warren, H. Rabitz, and M. Dahleh, *Science* **259**, 1581 (1993).
 - [18] M. Y. Kuchiev, *Pis'ma Zh. Eksp. Teor. Fiz.* **45**, 319 (1987) [*JETP Lett.* **45**, 404 (1987)].
 - [19] P. B. Corkum, *Phys. Rev. Lett.* **71**, 1994 (1993).

- [20] A. L'Huillier and P. Balcou, *Phys. Rev. Lett.* **70**, 774 (1993).
- [21] P. Agostini and L. F. DiMauro, *Rep. Prog. Phys.* **67**, 813 (2004).
- [22] H. Kapteyn, O. Cohen, I. Christov, and M. Murnane, *Science* **317**, 775 (2007).
- [23] F. Krausz and M. Ivanov, *Rev. Mod. Phys.* **81**, 163 (2009).
- [24] J. Ullrich, R. Moshhammer, A. Dorn, R. Dörner, L. P. H. Schmidt, and H. Schmidt-Böcking, *Rep. Prog. Phys.* **66**, 1463 (2003).
- [25] R. W. Robinett, *Phys. Rep.* **392**, 1 (2004).
- [26] A. S. Alnaser, B. Ulrich, X. M. Tong, I. V. Litvinyuk, C. M. Maharjan, P. Ranitovic, T. Osipov, R. Ali, S. Ghimire, Z. Chang, C. D. Lin, and C. L. Cocke, *Phys. Rev. A* **72**, 030702 (2005).
- [27] F. Légaré, K. F. Lee, I. V. Litvinyuk, P. W. Dooley, A. D. Bandrauk, D. M. Villeneuve, and P. B. Corkum, *Phys. Rev. A* **72**, 052717 (2005).
- [28] H. Niikura, D. M. Villeneuve, and P. B. Corkum, *Phys. Rev. A* **73**, 021402 (2006).
- [29] T. Ergler, A. Rudenko, B. Feuerstein, K. Zrost, C. D. Schröter, R. Moshhammer, and J. Ullrich, *Phys. Rev. Lett.* **97**, 193001 (2006).
- [30] B. Feuerstein, T. Ergler, A. Rudenko, K. Zrost, C. D. Schröter, R. Moshhammer, J. Ullrich, T. Niederhausen, and U. Thumm, *Phys. Rev. Lett.* **99**, 153002 (2007).
- [31] M. Magrakvelidze, F. He, T. Niederhausen, I. V. Litvinyuk, and U. Thumm, *Phys. Rev. A* **79**, 033410 (2009).
- [32] F. Kelkensberg, C. Lefebvre, W. Siu, O. Ghafur, T. T. Nguyen-Dang, O. Atabek, A. Keller, V. Serov, P. Johnsson, M. Swoboda, T. Remetter, A. L'Huillier, S. Zherebtsov, G. Sansone, E. Benedetti, F. Ferrari, M. Nisoli, F. Lépine, M. F. Kling, and M. J. J. Vrakking, *Phys. Rev. Lett.* **103**, 123005 (2009).
- [33] F. He and U. Thumm, *Phys. Rev. A* **81**, 053413 (2010).
- [34] M. D. Feit, J. A. Fleck, Jr., and A. Steiger, *J. Comput. Phys.* **47**, 412 (1982).
- [35] C. Lefebvre, T. T. Nguyen-Dang, F. Dion, M. J. J. Vrakking, V. N. Serov, and O. Atabek, *Phys. Rev. A* **88**, 053416 (2013).
- [36] See Supplemental Material at <http://link.aps.org/supplemental/10.1103/PhysRevA.93.012507> for supplemental movies visualizing the elevator mechanism.